

An Afterglow Study of the “New Year’s Burst” GRB 220101A

AGNIVA ROYCHOWDHURY ^{1,2} TUOMAS KANGAS ,^{3,4} ANDREW FRUCHTER ,² A. PE’ER ,⁵ K. BHIROMBAKDI ,^{2,6}
 J. GRAHAM ,⁷ K. MISRA ,⁸ A.J. LEVAN ,⁹ B. CENKO ,¹⁰ A. CUCCHIARA ,¹¹ V. CUNNINGHAM ,¹²
 B. P. GOMPERTZ ,^{13,14} D. PERLEY ,¹⁵ J. RACUSIN ,¹⁰ AND N. R. TANVIR ,¹⁶

¹National Centre for Radio Astrophysics - Tata Institute of Fundamental Research, Ganeshkhind, Pune 411007, MH, India

²Space Telescope Science Institute, 3700 San Martin Drive, Baltimore, MD 21218, USA

³Finnish Centre for Astronomy with ESO (FINCA), FI-20014 University of Turku, Finland

⁴Department of Physics and Astronomy, FI-20014 University of Turku, Finland

⁵Department of Physics, Bar Ilan University, Ramat-Gan 52900, Israel

⁶Lead Prompt Security Researcher | AI Safety & Red-Teaming at InjectPrompt

⁷Visitor, University of Hawaii at Manoa, 2505 Correa Rd, Honolulu, HI 96822

⁸Aryabhatta Research Institute of Observational Sciences, Manora Peak, Nainital 263001, India

⁹Department of Astrophysics/IMAPP, Radboud University Nijmegen, P.O. Box 9010, Nijmegen, 6500 GL, The Netherlands

¹⁰NASA Goddard Space Flight Center, Greenbelt, MD 20771, USA

¹¹NASA Headquarters, 300 E St. SW, Washington DC USA

¹²University of Maryland, College Park, MD 20742, USA

¹³School of Physics and Astronomy, University of Birmingham, Birmingham B15 2TT, United Kingdom

¹⁴Institute for Gravitational Wave Astronomy, University of Birmingham, Birmingham B15 2TT, United Kingdom

¹⁵Liverpool John Moores University (LJMU), 10 Copperas Hl, Liverpool L3 5AH, United Kingdom

¹⁶School of Physics and Astronomy, University of Leicester, University Rd, Leicester LE1 7RH, United Kingdom

ABSTRACT

We present a detailed broadband afterglow study of GRB 220101A ($10^4 \lesssim \Delta T \lesssim 10^7$ s) combining multi-wavelength data from soft X-rays until 6 GHz. The afterglow light curves in both X-ray and optical show distinct steepening around ~ 9 days, followed by a sharp post-break decay index of $\sim 2.99 \pm 0.10$. We fit the light curves using the afterglow modelling package `afterglowpy` for both Top-hat and Gaussian jets for different values of the electronic participation fraction ξ from 0.01 to 1.0 and find that, although the radio behavior is well described by the $\xi = 1.0$ case, the required circumburst medium (CBM) densities are very low, $< 10^{-4}$ cm⁻³. However, the resulting energy requirements are modest, $\sim 10^{52}$ erg, with an electron energy distribution (EED) index $p \sim 2.05$. Similar results are also obtained from an analytic model fit to the light curve, except the predicted p is higher, ~ 2.40 . The observed post-break decay index of 2.99 is at least 5σ away from p , which is one of the steepest observed so far. We also find that when ignoring the radio observations, the CBM density is raised by a few orders of magnitude to ~ 0.01 cm⁻³ for $\xi = 1.0$, still far from the expected ISM density (> 1 cm⁻³) of GRB environments, which are highly star forming regions. Similarly low ISM densities have been seen in modeling of other LAT GRBs as well, especially ones with reverse-shock features (e.g., GRBs 130427A, 160509A and 160625B), thereby hinting at either an issue with the standard model or possible evacuated cavities where GRBs explode.

1. INTRODUCTION

GRB 220101A is an extremely energetic long-duration gamma-ray burst (GRB) ($T_{90} = 173 \pm 13$ s; [Markwardt et al. 2022](#)) detected on New Year’s Day 2022 by *Swift* ([Tohuvavohu et al. 2022](#)). Spectroscopic studies deter-

mined its redshift to be $z = 4.618$ ([Fynbo et al. 2022](#)) and in combination with the measured Konus-Wind fluence, this implies an isotropic gamma-ray energy of $E_{\text{iso}} \simeq 3.6 \times 10^{54}$ erg ([Tsvetkova et al. 2022](#)), making this burst one of the most energetic ever detected (the 10th-most energetic listed in [Burns et al. 2023](#)). The burst was also detected by the *Fermi*-LAT instrument, and this allowed us to activate a Chandra X-ray Observatory program intended to study the most energetic

GRBs with the expectation that these bursts could potentially place limits on the nature of the engine behind the burst and the physics of the afterglow. The *Chandra* program also gave us access to the Hubble Space Telescope (*HST*) and the Karl G. Jansky Very Large Array (VLA). These observatories allow us to extend the study of this burst both in time and in wavelength compared to previous discussions (Zhu et al. 2023) and to follow the afterglow well after the jet break in spite of the afterglow declining as steeply (within the errors) as any other observed long gamma ray burst (LGRB).

In this paper, we analyze the broadband afterglow ($10^4 \lesssim \Delta T \lesssim 10^7$ s) of the GRB observed in the X-rays (with *Swift*-XRT and *Chandra*), optical-IR (with the *HST* and various ground based telescopes), and submm-radio with the Atacama Large Millimeter Array (ALMA) and the Karl G. Jansky Very Large Array (VLA). In Section 2, we discuss the data analyses and reduction. In Section 3, we conduct a numerical and analytical modelling of the broadband afterglow light curve. In Sections 4 and 5, we discuss our results in the context of GRB physics and how studies like these can open up avenues for better testing of the standard GRB model.

2. OBSERVATIONS AND DATA ANALYSIS

In this section, we present the set of multi-wavelength data obtained, reduced, and analyzed for this work, spanning from soft X-rays to cm-wave radio frequencies.

2.1. *X-rays*

2.1.1. *Swift* observations

Swift observed the prompt emission of GRB 220101A from 74 to 240s after outburst using the Windowed Timing (WT) mode of its X-ray Telescope (XRT). It returned to the GRB in Photon Counting (PC) mode starting at 3800s after the outburst. The PC data (along with other data we will discuss) are shown in Figure 1. The *Swift* data were obtained from the *Swift*/XRT lightcurve repository¹ (Evans et al. 2007, 2009). To convert counts in the full energy range to flux density at 5 keV, we used the parameters of the best *Swift*/XRT spectrum fit: a Galactic neutral hydrogen column density $N_{\text{H},\text{MW}} = 6.29 \times 10^{20} \text{ cm}^{-2}$, a photon index of $\Gamma_{X,\text{WT}} = 1.63$ and a host-galaxy neutral hydrogen column density of $N_{\text{H},\text{int}} = 6 \times 10^{21} \text{ cm}^{-2}$.² The conversion to flux density was performed using the web-based Portable Interactive Multi-Mission Simula-

tor (PIMMS³) tool which gives us a conversion factor of $3.882 \times 10^{-12} \text{ erg cm}^{-2} \text{ s}^{-1} \text{ keV}^{-1} \text{ count}^{-1}$.

2.1.2. *Chandra* Observations

After about thirteen days, GRB 220101A became too faint for *Swift*/XRT. Therefore, we observed GRB 220101A with the *Chandra* X-ray Observatory in five epochs between February 8 and February 10, 2022 (38 to 40 days after outburst) for a total exposure time of 74,300 s with a mean date of February 9.58 (39.4 days after outburst). These observations were performed under Proposal 23500404 (PI: Fruchter).

We obtained a clear detection of the GRB in the combined *Chandra* data. In an aperture of 3 pixels radius, which will contain 90% to 95% of the total flux depending on photon energy⁴, we detected 17 photons at the location of the GRB. Based on the measured background we would have expected one photon in the aperture in the absence of a source. Again using the PIMMS calculator with the Swift parameters, and accounting both for the background and aperture correction, we find an unabsorbed flux density of $3.6_{-0.9}^{+0.9} \times 10^{-16} \text{ erg cm}^{-2} \text{ s}^{-1} \text{ keV}^{-1}$ where the error is dominated by the $\sim 25\%$ Poisson error of the source.

2.2. *Optical/IR*

2.2.1. *HST*

We observed the afterglow emission of GRB 220101A with the *HST* under proposal ID 16838 (PI : A. Fruchter), which was awarded through our *Chandra* program. We used the WFC3 in the nIR F125W filter, roughly equivalent to the ground-based *J* band, and in the nIR/optical F775W, which is close to the ground-based *i* band. We observed twice, first on February 7, 2022, \sim a month from the burst, and again on August 25, 2022, or nearly 9 months after the burst.

In both epochs, a single orbit was devoted to each filter, with four exposures taken in four-point dither patterns. The exposures were combined using `astrodrizzle` in the `Drizzlepac` library from STScI onto subsampled output images with pixel scales of $0.^{\prime\prime}02$ in the F775W filter and $0.^{\prime\prime}06$ in the F125W filter. To obtain the measurement of the optical transient's magnitude at the first epoch without contamination by a possible host, the two epochs were aligned using stars in the field and the second epoch was subtracted from the first. As the transient was fading as $\sim t^{-3}$ (see Sect. 3.1), any source flux remaining in the second

¹ <http://www.swift.ac.uk/xrt.curves/>

² https://www.swift.ac.uk/xrt_spectra/01091527/

³ <https://cxc.harvard.edu/toolkit/pimms.jsp>

⁴ <https://cxc.harvard.edu/proposer/POG/html/>

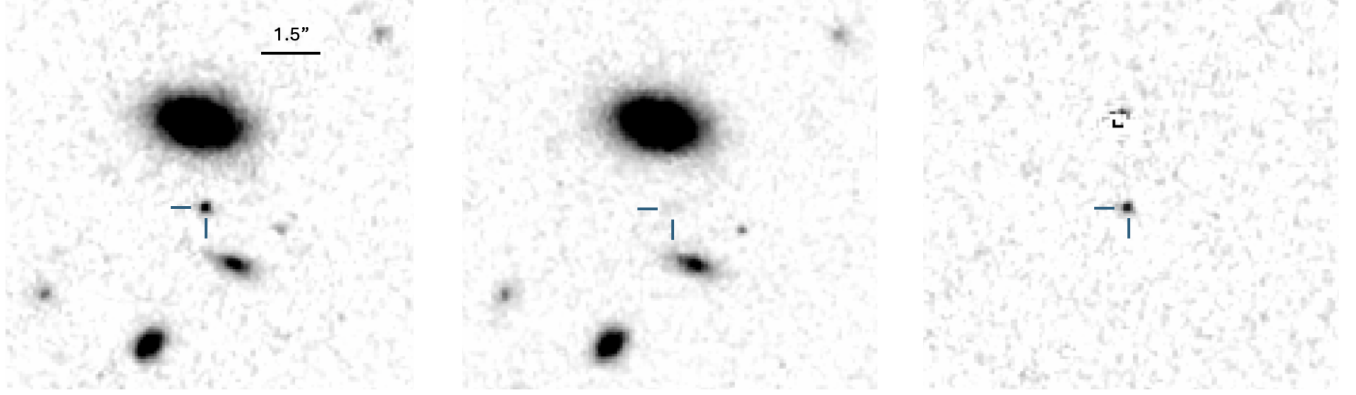


Figure 1. HST F125W image of the GRB 220101A. The two blue lines mark the position of the transient. Left : at ~ 38 days; Middle: at ~ 236 days; Right: background subtracted image at ~ 38 days.

epoch should introduce at most a negligible error in the subtraction. For February 7, 2022 we obtain AB magnitudes of 26.71 ± 0.13 in F775W and 25.65 ± 0.05 in F125W. The host-galaxy could not be significantly detected due to contamination from two nearby galaxies straddling the GRB (Figure 1).

2.2.2. *Ground-based optical/IR data*

Ground-based optical and nIR detections of the afterglow of GRB 220101A were reported by various observers through the NASA General Coordinates Network (GCN)⁵. In addition, follow-up data from several different telescopes and not included in the GCNs were published by Zhu et al. (2023). However, because of the high redshift of GRB 220101A ($z = 4.618$), the rest-frame Ly α line falls on 6830 Å. Therefore, the observed optical data in r/R and all bluer bands are affected by the Ly α forest. This effect on the optical spectrum was demonstrated by Zhu et al. (2023). Furthermore, the data at these bands do not include any points after the jet break (see Sect. 3.1). For these reasons, we ignore them in the following analysis and only use data in $i/F775W$ and redder bands. We use observations from GCNs 31353 (Fu et al. 2022), 31357 (Perley 2022a), 31358 (de Ugarte Postigo et al. 2022), 31361 (Vinko et al. 2022), 31373 (D’Avanzo et al. 2022a), 31395 (D’Avanzo et al. 2022b), 31401 (Nicuera Guelbenzu et al. 2022), 31425 (Perley 2022b); and all other photometry in these bands included in Zhu et al. (2023).

2.3. *Radio : VLA*

GRB220101A was observed by the VLA in 2022 under project ID SN0404 (PI: A. Fruchter) between 13th January and 3rd May and under project ID 21A-405 (PI: T.

Laskar) between 4th January and 12th March, through continued monitoring at 5 GHz to 34 GHz. We used the calibrated data directly if available, while for others the raw data was downloaded from the NRAO data archive⁶ and processed by the CASA 6.5.4 pipeline. The CASA task `tclean` (with natural weighting) was run on all the calibrated measurement sets at every observed frequency and the peak flux density (or equivalently the total since it was a point source) of the map was noted. Self-calibration was avoided due to low flux densities ($\lesssim 1$ mJy). Table 1 lists the band/frequency and date for each observation and the observed flux densities and the observed RMS sensitivity in each band.

2.4. *Sub-mm : ALMA*

The Atacama Large sub-Millimeter Array (ALMA) observed GRB220101A from 2022-01-02 to 2022-01-22 at Band 3 (97 GHz) under project ID 2021.1.00658.T (PI: T. Laskar). The calibrated data for each project were downloaded from the ALMA data archive⁷ and the task `tclean` with natural weighting was run on each measurement set. The resulting total flux densities at each frequency were noted for each observation and have been tabulated in Table 1 along with the VLA observations.

3. MODELLING AND ANALYSIS

This section aims to investigate the physical nature of the GRB 220101A afterglow through multi-wavelength light curve analysis and modelling using `afterglowpy` (Ryan et al. 2020) and an analytical fitting code (Kangas & Fruchter 2021) based on Granot & Sari (2002). As per the standard model (Mészáros & Rees 1999),

⁵ <https://gcn.nasa.gov/>

⁶ <http://data.nrao.edu>

⁷ <https://almascience.nrao.edu/>

Obs	Array	Freq. (GHz)	Project	Date YYYY-MM-DD	Phase (t) (days)	F_{tot} (mJy)	RMS (mJy)
VLA	A	6.0	21A-241	2022-01-04	2.9	0.182	0.010
"	"	6.0	21A-241	2022-01-08	6.9	0.322	0.009
"	"	6.0	SN0404	2022-01-13	11.9	0.312	0.009
"	"	6.0	21A-241	2022-01-14	12.9	0.201	0.011
"	"	6.0	21A-241	2022-01-15	13.9	0.261	0.013
"	"	6.0	SN0404	2022-01-22	20.9	0.220	0.010
"	"	6.0	21A-241	2022-01-29	27.9	0.120	0.009
"	"	6.0	SN0404	2022-02-08	37.9	0.060	0.007
"	"	6.0	SN0404	2022-03-05	62.9	0.050	0.004
"	"	6.0	21A-241	2022-03-12	69.9	0.039	0.009
"	"	10.0	"	"	2.9	0.323	0.008
"	"	10.0	"	"	6.9	0.458	0.009
"	"	10.0	"	"	11.9	0.467	0.008
"	"	10.0	"	"	12.9	0.262	0.011
"	"	10.0	"	"	13.9	0.300	0.011
"	"	10.0	"	"	20.9	0.230	0.010
"	"	10.0	"	"	27.9	0.122	0.010
"	"	10.0	"	"	37.9	0.056	0.005
"	"	10.0	"	"	62.9	0.038	0.003
"	"	10.0	"	"	67.9	0.042	0.009
"	"	10.0	SN0404	2022-04-29 - 2022-03-05	123.0	0.013	0.001
"	"	15.0	"	"	2.9	0.447	0.009
"	"	15.0	"	"	6.9	0.450	0.007
"	"	15.0	"	"	11.9	0.402	0.008
"	"	15.0	"	"	12.9	0.277	0.011
"	"	15.0	"	"	13.9	0.298	0.011
"	"	15.0	"	"	20.9	0.180	0.010
"	"	15.0	"	"	27.9	0.134	0.011
"	"	22.0	"	"	2.9	0.573	0.010
"	"	22.0	"	"	11.9	0.317	0.009
"	"	22.0	"	"	12.9	0.282	0.014
"	"	22.0	"	"	13.9	0.227	0.014
"	"	22.0	"	"	20.9	0.180	0.011
"	"	22.0	"	"	27.9	0.109	0.010
"	"	22.0	"	"	37.9	0.050	0.006
"	"	34.0	"	"	2.9	0.601	0.014
"	"	34.0	"	"	11.9	0.295	0.014
"	"	34.0	"	"	12.9	0.245	0.020
"	"	34.0	"	"	13.9	0.170	0.017
"	"	34.0	"	"	20.9	0.065	0.017
ALMA	12m	97 GHz	2021.1.00658.T	2022-01-02	0.9	0.810	0.012
ALMA	12m	97 GHz	"	2022-01-04	2.9	0.552	0.014
ALMA	12m	97 GHz	"	2022-01-08	6.9	0.310	0.017
ALMA	12m	97 GHz	"	2022-01-22	20.9	0.122	0.018

Table 1. Table lists the summary of all radio-submm observations used in this paper: the telescope and array used, the project ID, the observing frequency and date, the total flux density and RMS. The phase column refers to the time elapsed since the burst.

GRB afterglow emission is a result of a highly relativistic jet ($\Gamma \gtrsim 100$) shocking the CBM to drive a forward shock into the CBM and a reverse shock back into the ejecta to accelerate electrons in both media. The focus of this work is on examining the behavior of the forward shock and, particularly, the geometric jet break. This is a highly time-dependent radiation calculation that includes the time evolution of relevant synchrotron frequencies and the geometric effects of the jet as it decelerates. An afterglow light curve at any given wavelength is generally observed to contain a series of power-law segments between breaks. Each break is observed as a change in light curve slope as the break frequency of the synchrotron emission spectrum moves through the observed frequency. The expected breaks in slope are related to the passing of the self-absorption break (or ν_{sa}), the cooling break (ν_c) and the base synchrotron frequency (ν_m). The sequence of these breaks depends on the external environment, the observing frequency and the physical properties of the GRB.

In addition to all these breaks, a GRB afterglow can, at late times, display a decay slope that is steeper than the expected slopes from all the synchrotron breaks and which is achromatic across much of the spectrum. This occurs when the continuous deceleration of the jet leads to the relativistic beaming of the light becoming broader than the opening angle of the jet ($\Gamma < 1/\theta_j$). Until this point, while the surface brightness of the jet has fallen as the relativistic beaming angle increased, the area of the jet the observer sees has grown as well. However, this offset stops abruptly when the relativistic beaming becomes broader than the jet itself, producing a dramatic steepening of the light curve (Mészáros & Rees 1999; Sari et al. 1999). In addition, lateral expansion of the jet at the speed of sound can further steepen the decline to a post-break slope of $-p$, where p is the power-law slope of the energies of the synchrotron electrons (Rhoads 1999). As we will discuss later, these analytical expectations can be altered by energy injection and hydrodynamic effects.

3.1. Light Curve Analysis

Most of the underlying physics in GRB afterglow light curves can be understood by studying the nature of their broadband power law indices and the presence/absence of break(s). For simplicity of discussion, we start by showing in Figure 2 only the extinction-corrected ground-based *i*-band and HST F814W observations along with the X-ray data from XRT and Chandra. The X-ray and the optical light curves in Figure 2 show a distinct geometric jet break at $\lesssim 10$ days. We fit

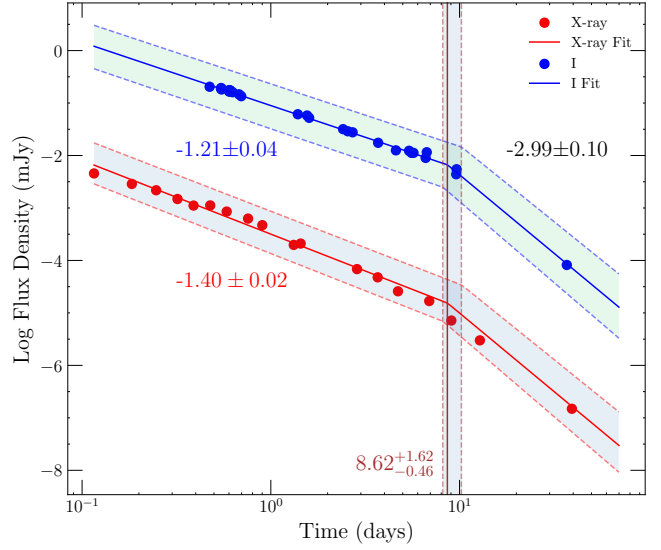


Figure 2. Figure showing the I band and the X-ray points, which were sampled the most among all wavelengths, and the results of the broken power law fit using Equation 1.

the X-ray and optical using a broken power law of the following form:

$$F_\nu(t) = A \left[\left(\frac{t}{t_j} \right)^{-\omega \alpha_L} + \left(\frac{t}{t_j} \right)^{-\omega \alpha_H} \right]^{-1/\omega} \quad (1)$$

where A is a normalization parameter, t_j is the break timescale, α_L and α_H are the pre (“low”) and post-break (“high”) slopes respectively, and ω denotes the break sharpness, with $\omega = 1$ and $\omega \gg 1$ implying minimum and maximum sharpness respectively. As the post-jet-break slopes and timescales are expected to be achromatic (for all cases other than $\nu < \nu_m < \nu_c$), we assume the same break parameters for both light curves except the pre-break slope. Figure 2 shows the fit with a $\omega = 10$, which provides a sharp break. The fit was done using the `emcee` (Foreman-Mackey et al. 2013) Markov-chain Monte Carlo (MCMC) package and the resulting best-fit parameters (medians and one sigma values) are displayed in the figure.

The pre-break slopes for the optical and X-rays are -1.21 ± 0.04 and -1.40 ± 0.02 , respectively. They differ by $\sim 0.19 \pm 0.05$, whose 1σ limit, ~ 0.24 , is close to $\Delta \alpha_{X-O} = 0.25$, expected when the cooling frequency lies between the optical and the X-rays in a constant-density circumburst medium (CBM) with $\nu_m < \nu < \nu_c$ or $\nu_m, \nu_c < \nu$ (c.f. Granot & Sari 2002). This implies the pre-break indices for the two frequency regimes would be given by $\alpha_X = -(3p_X - 2)/4$ and $\alpha_O = -3(p_O - 1)/4$ and hence $\Delta \alpha_{X-O} = 0.25$, according to theoretical expectations. Plugging the observed values of α_O and α_X , we obtain $p = p_O \sim 2.61 \pm 0.03$ and $p = p_X \sim 2.86 \pm 0.05$,

whose 1σ limits are close (2.64 and 2.80 respectively). The post-break slope, in contrast, is -2.99 ± 0.10 . While the break timescale is ~ 8.62 days as evident from the figure, the post-break slope is markedly steep. The analytic expectation from a jet that expands sideways after the jet break is a post-break index of p implying if the spectral model fits provide a value of $p \sim 3.0$, we would be able to confirm lateral expansion. The afterglow models have been discussed in upcoming sections and possibilities of lateral expansion dealt with. The differences between these three post-break slopes (p_O, p_X assuming lateral expansion and 2.99 ± 0.10) are non-negligible, but compatible with the findings of [Gompertz et al. \(2018\)](#), who found a scatter of $\sigma_p \approx 0.25$ when obtaining p through different relations for the same GRBs. One should also note that due to the poor sampling of data points around and beyond the jet break, the break timescale and the post-break slopes are correlated and underconstrained. For example, an earlier break time would result in a slightly flatter post-break index and vice versa. It is also possible that we are seeing effects of hydrodynamics that are not captured in usual analytical calculations.

The radio frequency points have been plotted separately in Figure 3 to reduce clutter. While it seems that the radio behaviour does not resemble a broken power law, diffraction and refractive scintillation may cause large enough fluctuations in flux density ($\sim 50\%$) to cause a departure from a smooth power law. There is lack of a clear unifying feature among all frequencies except a possible general steepening after ~ 10 days. It is possible that the peak synchrotron frequency (ν_m) moves through the radio frequencies at $\lesssim 10$ days.

3.2. Afterglow spectral and light curve modeling

Afterglows can be modelled either through analytical theory or using sophisticated hydrodynamic simulations. As introduced earlier, `afterglowpy` is a numerical code that balances both these techniques ([Ryan et al. 2020](#)) and which approximates hydrodynamics through calibration to the more rigorous `BOXFIT` ([van Eerten et al. 2012](#)) that includes complete hydrodynamic simulations. To model our light curves, we chose `afterglowpy` for its ease of use and speed.

While modelling the afterglow, the initial choice of the jet model is important because of viewing angle effects. A structureless, top-hat jet that has a uniform energy profile should produce distinctly different emission patterns from a structured (say, Gaussian) jet that has a different energy cross-section. This effect would be more pronounced if the viewing angle is larger than the jet opening angle, more likely for narrower and faster jets.

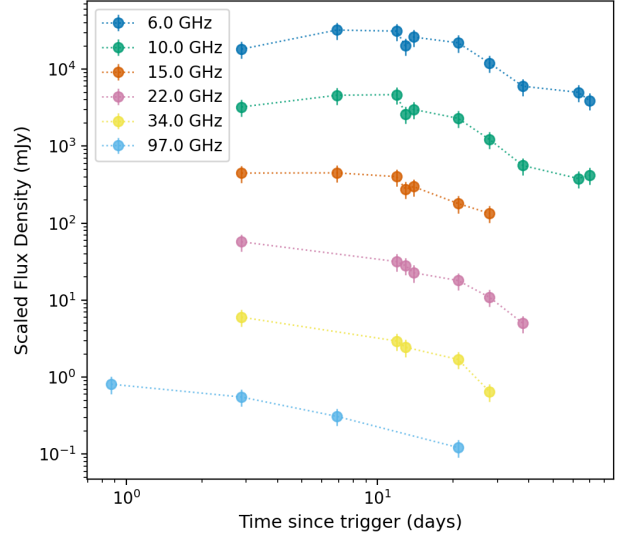


Figure 3. Radio to submm light curves plotted separately (scaled accordingly) for better clarity. While no clear smooth/broken power law behaviour is evident like optical and X-rays, a general change in trend after 10 days is evident for the 6 – 10 GHz light curves.

For this work, we used both a top-hat and a Gaussian jet model in an ISM-like circumburst medium (CBM). Note that both models are only approximations and the jet shape is expected to evolve according to the physics of the GRB engine and the hydrodynamics of the flow through the CBM.

Since `afterglowpy` has no internal fitting algorithm, we wrote an MCMC wrapper using `emcee`, which we gave uniform/log-uniform priors on all relevant parameters (described in Table 6) and tasked it to optimize the χ^2 . Since the resulting posterior distributions(s) peaked around the median, we took the median of the resulting posterior distribution of each parameter as the final best-fit value and the 16th and 84th percentiles as one-sigma errors. The free parameters included the total isotropic-equivalent kinetic energy E_{iso} , the electron energy distribution (EED) spectral index p , the viewing and opening angles θ_{obs} and θ_j , the CBM density n_0 and the fraction of internal energy in electrons and magnetic fields as ϵ_e and ϵ_B respectively. We added host-galaxy extinction correction through A_B using the extinction laws of [Pei \(1992\)](#). We ran `afterglowpy` for two cases of the electron participation fraction ξ (the fraction of thermal electrons that are accelerated to non-thermal energies and thus take part in the synchrotron radiation) at 0.1 and 1.0, where respectively 10% and 100% of the electrons radiate. While for a large enough number of MCMC steps (8000 here) and walkers (800 here) the choice of the initial conditions is immaterial,

Parameter (unit)	Prior	Range
$E_{\text{K,iso}}$ (erg)	Log-uniform	[52.0:57.0]
p	Uniform	[2.0:3.0]
n_0 (cm $^{-3}$)	Uniform	[10^{-6} :2.0]
θ_j (rad)	Uniform	[10^{-4} :0.5]
θ_{obs} (rad)	Uniform	[10^{-4} :0.5]
ϵ_e	Uniform	[10^{-5} :1]
ϵ_B	Uniform	[10^{-5} :1]
A_B (mag)	Uniform	[0:5]

Table 2. Parameters and priors of our `afterglowpy` fits.

we provided an initial prior based on a *trial and error* `afterglowpy` fit to the light curve and thereafter used the median of the initial posterior as the initial values for all subsequent MCMC runs for the source.

For each fit, we binned the X-ray light curve, taking the average epoch and flux in each time bin of 0.1 dex starting from the first PC-mode observation. We furthermore added a 10 per cent error floor in the X-ray and optical light curves and 25 per cent in the radio. This was done in order to reduce the overweighing produced by the large number of *Swift* X-ray points, and to prioritize a good fit in the late-time optical and X-ray over the radio (see Sect. 4). Additionally, the radio de-weighting helps account for the scatter in radio points caused by refractive and diffractive scintillation.

3.2.1. Top-hat Jet

A top-hat jet is a simple jet model frequently used in simulations/numerical calculations. It has a uniform energy across its cross section and zero beyond, that is $E(\theta) = E(\theta = 0)$ for $\theta \leq \theta_j$ and $E(\theta) = 0$ for $\theta > \theta_j$, where θ is the angle between the jet axis and a line drawn to a piece of the jet from the bottom of the jet axis, and θ_j denotes the jet-edge.

Table 3 lists the median best-fit parameters for the Top-Hat jet from the MCMC fit for each of the two participation fractions. While it is expected that with higher electron participation fractions both the total required energy and the required CBM density (or the CBM mass that needs to be shocked keeping the same volume) will drop, we find that for $\xi = 1.0$ the CBM density drops extremely low, to $\sim 10^{-5}$ cm $^{-3}$. ISM density posteriors lower than 10 $^{-4}$ cm $^{-3}$ are, perhaps surprisingly, not uncommon when fitting multi-wavelength afterglows (e.g., Kangas et al. 2020; Kangas & Fruchter 2021; Cunningham et al. 2020) but it is unclear how physical such a value is. Zhu et al. (2023) obtained different best-fit parameters though, and in Appendix A we try to bridge the differences in the best-fits between Zhu et al. (2023) and ourselves.

Parameter	$\xi = 0.1$	$\xi = 1.0$
$\log(E_{\text{K,iso}}/\text{erg})$	$56.28^{+0.28}_{-0.31}$	$56.17^{+0.07}_{-0.05}$
p	2.02 ± 0.01	2.16 ± 0.02
$\log(\theta_{\text{obs}}/\text{rad})$	$-2.22^{+0.04}_{-0.05}$	-2.45 ± 0.04
$\log(\theta_j/\text{rad})$	$-1.98^{+0.06}_{-0.04}$	-2.19 ± 0.03
$\log(n_0/\text{cm}^{-3})$	$-2.39^{+0.50}_{-0.70}$	$-5.44^{+0.25}_{-0.33}$
$\log \epsilon_e$	$-0.20^{+0.18}_{-0.35}$	$-1.38^{+0.11}_{-0.09}$
$\log \epsilon_B$	$-1.72^{+0.56}_{-0.29}$	$-1.84^{+0.34}_{-0.31}$
A_B (mag)	$0.46^{+0.15}_{-0.21}$	$0.13^{+0.04}_{-0.02}$
E_{K} (erg)	1.0×10^{52}	3.1×10^{51}
χ^2/DOF	8.80	2.12

Table 3. Best-fit parameters for the Top-hat jet for different values of ξ .

Figure 4 shows the resulting light curve fits for $\xi = 0.1$ and 1.0. While the X-ray observations are well fit by our model irrespective of ξ , the behaviour of both the optical/IR and the radio fit depends on ξ . Only at high ξ do we see a general similarity in tendency between the data and the model, more so for the radio. For the optical/IR, even the pre-break light curve decay is only captured by the model at $\xi = 1.0$. A higher ξ also produces a larger jet opening angle, and the jet-break timescale is very sensitive to the opening angle: $t_B \propto (E_{\text{K,iso}}/n_0)^{1/3} \theta_j^{8/3}$ (Sari et al. 1999). As evident in Table 3 and 3.2.1, the larger opening angle has shifted the predicted break timescale to lower values, thereby fitting the radio better. Accordingly, the lowest chi-squared we obtain is for $\xi = 1.0$, as shown in Table 3.

The cooling frequency ν_c is different at different values of ξ , as evident from our Top-hat model spectra shown in Figure 5. The kink in the figure is due to the Heaviside-like extinction correction applied to the optical bands. ν_c lies between the optical and the X-rays for the entire duration of the afterglow at $\xi = 1.0$. This is consistent with the power-law slopes shown in Fig. 2. However, for $\xi = 0.1$, we observe that the cooling frequency stays less than the optical frequencies ($\nu_c \lesssim 10^{14}$ Hz) after ~ 5 days evident in Figure 5.

We also note that `afterglowpy` does not incorporate synchrotron self-absorption as of yet in the latest version, due to the fact that ν_{sa} is generally much lower than the observed radio frequencies during most of the afterglow emission (**pvt comm.**). For example, the self-absorption frequency for slow cooling ($\nu_c > \nu_m$) in a constant density CBM is given as (Granot et al. 2000) :

$$\nu_{\text{sa}} = 1.24 \times 10^9 (1+z)^{-1} \epsilon_e^{-1} \epsilon_B^{1/5} n_0^{3/5} E_{52}^{1/5} \frac{(p-1)^{3/5}}{(3p+2)^{3/5}} \text{Hz} \quad (2)$$

Plugging in values from Table 3 at $\xi = 0.1$, $\nu_{\text{sa}} \simeq 6$ MHz; estimated values are even lower for higher ξ . However, in the case of a burst with a high surrounding ISM

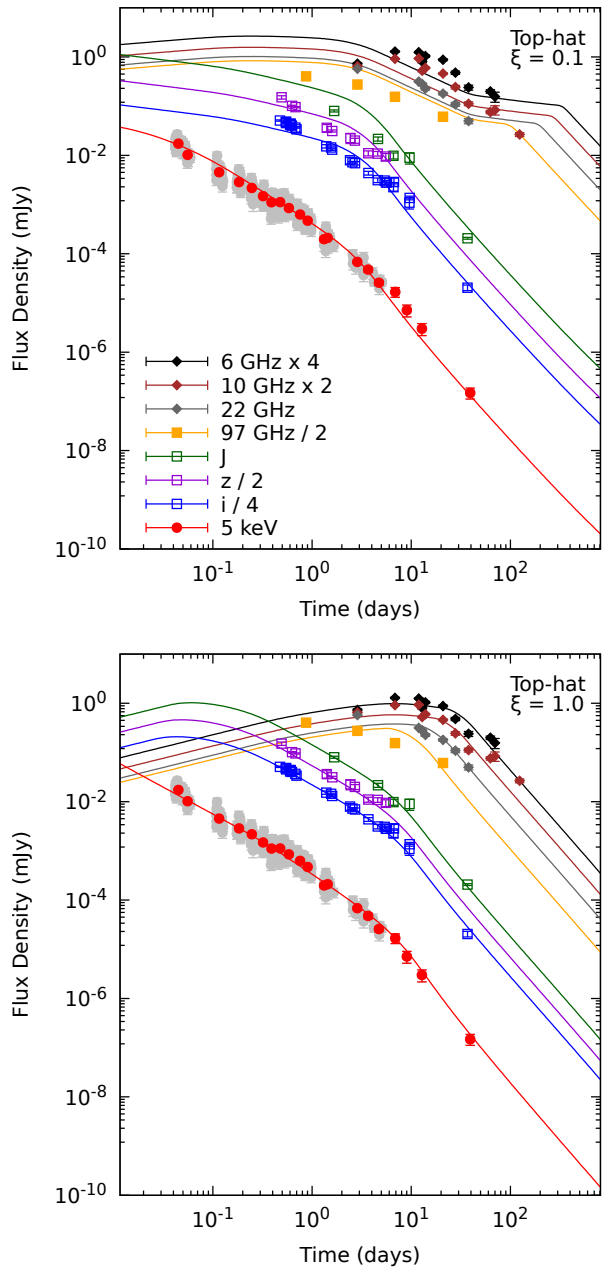


Figure 4. Afterglowpy top-hat jet fits to the light curves for $\xi = 0.1$ and $\xi = 1.0$. Both the optical/IR and the radio data are fit better with the higher ξ . The grey points show the unbinned X-ray data.

density, at early times one might expect some lower-energy radio frequencies to be below ν_{sa} , where self-absorption would be important.

3.2.2. Gaussian Jet

A Gaussian jet is a structured jet, implying its energy varies across the jet and is a Gaussian function of θ . This is given as $E(\theta) = E_{iso}e^{-\theta^2/2\theta_j^2}$ for $\theta \leq \theta_W$ and $E(\theta) = 0$ otherwise, where θ_W is a defined jet edge, or

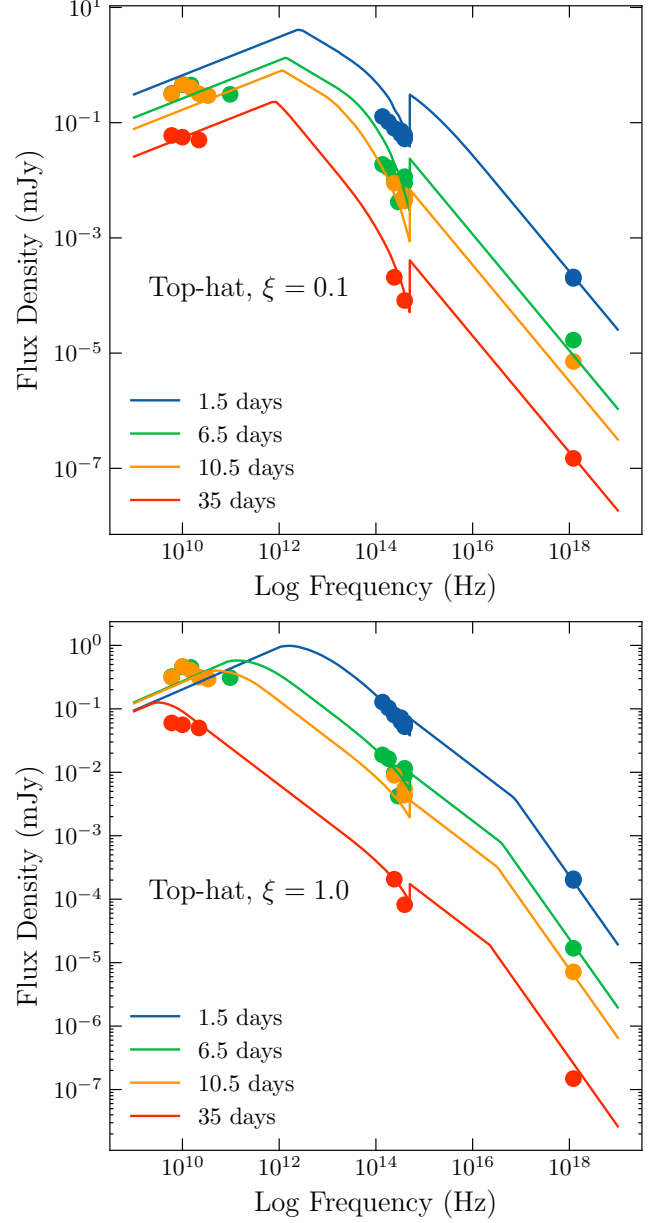


Figure 5. Afterglowpy spectral evolution for $\xi = 0.1$ and $\xi = 1.0$ with the top-hat jet. The evolution of the break frequencies is considerably different between the two models, and the $\xi = 1.0$ model fits the X-ray evolution better. The kink in the figures is due to the Heaviside-like (step function in frequency) extinction correction applied to the optical bands.

where the Gaussian wing is truncated. Here we choose $\theta_W = 4\theta_j$ which has been used typically in literature, generally to be the maximum width of the jet (see e.g., van Eerten et al. 2024).

Table 4 lists the median best-fit parameters for the Gaussian jet from the MCMC fit for each of the par-

Parameter	$\xi = 0.1$	$\xi = 1.0$
$\log(E_{K,\text{iso}}/\text{erg})$	$56.21_{-0.12}^{+0.19}$	$56.36_{-1.03}^{+0.11}$
p	$2.01_{-0.00}^{+0.00}$	$2.12_{-0.08}^{+0.05}$
$\log(\theta_{\text{obs}}/\text{rad})$	$-2.19_{-0.04}^{+0.03}$	$-2.32_{-0.04}^{+0.24}$
$\log(\theta_c/\text{rad})$	$-2.18_{-0.04}^{+0.04}$	$-2.28_{-0.04}^{+0.16}$
$\log(n_0/\text{cm}^{-3})$	$-2.61_{-0.39}^{+0.35}$	$-4.93_{-0.06}^{+1.26}$
$\log \epsilon_e$	$-0.04_{-0.07}^{+0.07}$	$-1.12_{-0.12}^{+1.11}$
$\log \epsilon_B$	$-0.76_{-0.74}^{+0.58}$	$-2.20_{-0.32}^{+2.12}$
A_B (mag)	$0.37_{-0.02}^{+0.03}$	$0.20_{-0.06}^{+0.41}$
E_K (erg)	3.5×10^{51}	3.2×10^{51}
χ^2/DOF	8.56	4.77

Table 4. Best-fit parameters for the Gaussian jet for different values of ξ , with values taken from the provided corner plots.

Parameter	$\xi = 1.0$
$\log(E_{K,\text{iso}}/\text{erg})$	$56.53_{-0.23}^{+0.08}$
p	$2.04_{-0.01}^{+0.01}$
$\log(\theta_{\text{obs}}/\text{rad})$	$-1.83_{-0.08}^{+0.08}$
$\log(\theta_j/\text{rad})$	$-1.62_{-0.09}^{+0.08}$
$\log(n_0/\text{cm}^{-3})$	$-0.44_{-0.52}^{+0.50}$
$\log \epsilon_e$	$-0.02_{-0.01}^{+0.01}$
$\log \epsilon_B$	$-3.37_{-0.44}^{+0.50}$
A_B (mag)	$0.71_{-0.01}^{+0.01}$

Table 5. Best-fit parameters for the Top-hat jet fits ignoring or extremely underweighting radio observations.

ticipation fractions listed. Most of the parameters are similar to those of the top-hat jet model.

Figure 6 shows the resulting light curve fits for $\xi = 0.1$ and 1.0. The fit behaviour is very similar to the Top-hat case, implying the fit results are not sensitive to the presence or absence of a structured jet.

3.2.3. Fit excluding radio observations and the case of GRB 160625B

Here we investigate to what extent the resulting GRB parameters for GRB220101A are driven by the radio behavior. Figure 7 shows the resulting plot from only fitting the X-rays and the optical. The expected radio emission is almost an order of magnitude higher than what is observed when $\xi = 1.0$, despite fitting the observations fairly well when they are included in the fit. Further, Table 5 shows the resulting best-fit parameters at $\xi = 1.0$ for a top-hat jet when radio points are excluded from the fit. Interestingly, the predicted ISM density is much higher, ~ 100 times larger, when the radio is neglected.

The radio afterglow of GRB 160625B has shown similar behavior. Kangas et al. (2020) and Kangas & Fruchter (2021) noted that this GRB's radio emission

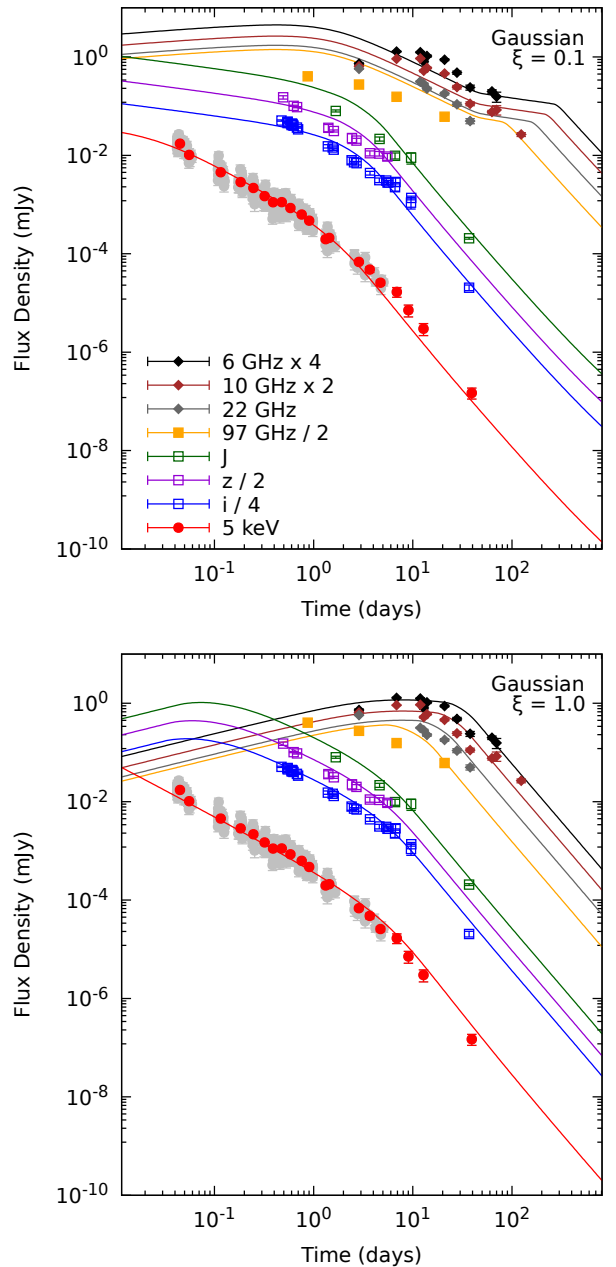


Figure 6. Afterglowpy Gaussian jet fits to the light curves for $\xi = 0.1$ and $\xi = 1.0$. Both the optical/IR and the radio data are fit better with the higher ξ .

differed from predictions of the standard model, and numerical and analytical models failed to reproduce the late-time radio behavior. In addition, its CBM density was noted to also be on the order of 10^{-5} cm^{-3} (Cunningham et al. 2020; Kangas et al. 2020). In Appendix B, we include a test similar to the above, and show that removing the radio from the fit of GRB 160125B increases the estimated CBM density by more than an order of magnitude.

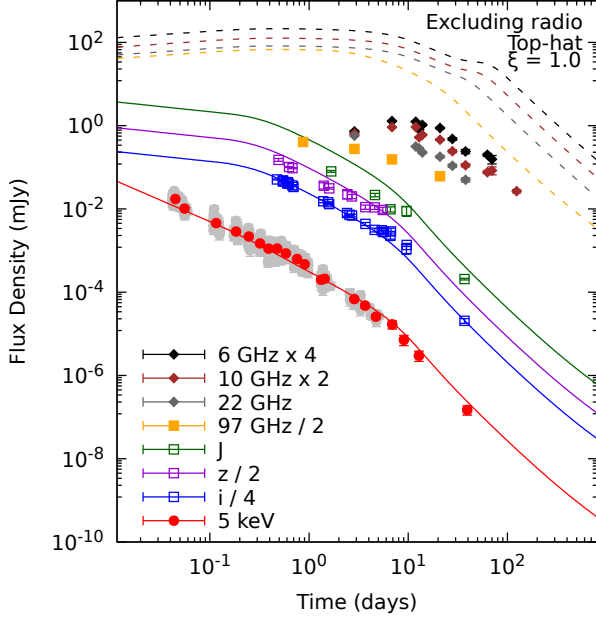


Figure 7. Afterglowpy top-hat jet $\xi = 1.0$ light curve without using radio (dashed lines) in the fit.

3.3. Analytical fit

Since `afterglowpy` lacks a wind-type CBM treatment and does not incorporate synchrotron self-absorption (Ryan et al. 2020), we also used an analytical code implementing the spectrum of a top-hat jet afterglow in ISM- and wind-type CBM (Granot & Sari 2002). This custom python-based MCMC code was originally written for the analysis of a sample of multi-wavelength afterglows in Kangas & Fruchter (2021). The code uses the `emcee` package and includes implementations of inverse Compton radiation (Sari & Esin 2001) and jet breaks with and without lateral expansion (Mészáros & Rees 1999; Rhoads 1999). For a more detailed description of the modeling code, see Kangas & Fruchter (2021). The free parameters, similar to those of the `afterglowpy` fit, include θ_j , $E_{K,\text{iso}}$, n_0 (ISM-type CBM) or the dimensionless density parameter A_* (wind-type CBM), p , ϵ_e , ϵ_B and A_B . We again adopted wide, uniform or log-uniform prior ranges for each parameter, with 10 or 25 per cent error floors in optical/X-ray and radio bands respectively. The parameters and their prior ranges are listed in Table 6, while the median posterior parameters and their uncertainties are listed in Table 7. The best fits are shown in Fig. 8.

The wind model fails to replicate the late-time decline. The best ISM fit is better in terms of χ^2 , and matches the observations in the radio and optical reasonably well, while the X-ray decline by eye is slightly too shallow both before and after the break. This is because the

model puts ν_c above 5 keV until the last observed epoch, while our power-law fits indicate this is not the case (see Sect. 3.1). Additionally, the best ISM fit again includes an extremely low density – on the same order as the `afterglowpy` fit with $\xi = 1.0$ described above. Both fits additionally have an extremely narrow jet opening angle at the edge of the prior.

Parameter (unit)	Prior	Range
θ_j (rad)	Log-uniform	$[0.01:0.5]$
$E_{K,\text{iso}}$ (erg)	Log-uniform	$[10^{49}:10^{57}]$
n_0 (cm^{-3}) or A_*	Log-uniform	$[10^{-6}:10^5]$
p	Uniform	$[2.0:3.2]$
ϵ_e	Log-uniform	$[10^{-5}:1]$
ϵ_B	Log-uniform	$[10^{-5}:1]$
A_B (mag)	Uniform	$[0:5]$

Table 6. Parameters and priors of our analytical afterglow fits.

Parameter (unit)	ISM	Wind
$\log (E_{K,\text{iso}}/\text{erg})$	$56.04^{+0.07}_{-0.11}$	55.47 ± 0.04
p	$2.41^{+0.02}_{-0.03}$	2.18 ± 0.02
$\log (\theta_j/\text{rad})$	$-1.994^{+0.009}_{-0.002}$	$-1.997^{+0.006}_{-0.003}$
$\log (n_0/\text{cm}^{-3})$ or $\log A_*$	$-5.16^{+0.16}_{-0.07}$	-1.67 ± 0.04
$\log \epsilon_e$	$-1.54^{+0.06}_{-0.03}$	-1.44 ± 0.02
$\log \epsilon_B$	$-2.02^{+0.23}_{-0.20}$	-1.33 ± 0.10
A_B (mag)	0.13 ± 0.02	0.19 ± 0.02
χ^2/DOF	4.6	5.8

Table 7. Parameter posterior distributions in our best analytical afterglow fits.

4. DISCUSSION

4.1. Nature of the post-break light curve : sideways expansion or a geometric effect?

In the absence of instabilities, a collimated conical jet is confined by the external medium, with strict pressure boundary conditions defined along its boundary (e.g., Daly & Marscher 1988). This defines the typical jet “size” and its opening angle θ_j . As the jet decelerates by interaction with its medium, the luminosity typically decreases. An achromatic break in the jet light curve arises when the size of the beaming cone exceeds that permitted by the size of the jet, or the beaming angle exceeds the jet opening angle ($1/\Gamma > \theta_j$), after which the rate of decrease in luminosity is even faster since now in addition to the decrease in Γ , the observed luminosity is increasingly a smaller fraction (s_Ω/s_Γ , where s refers to the angular size of the relevant cone and s_Γ increases in

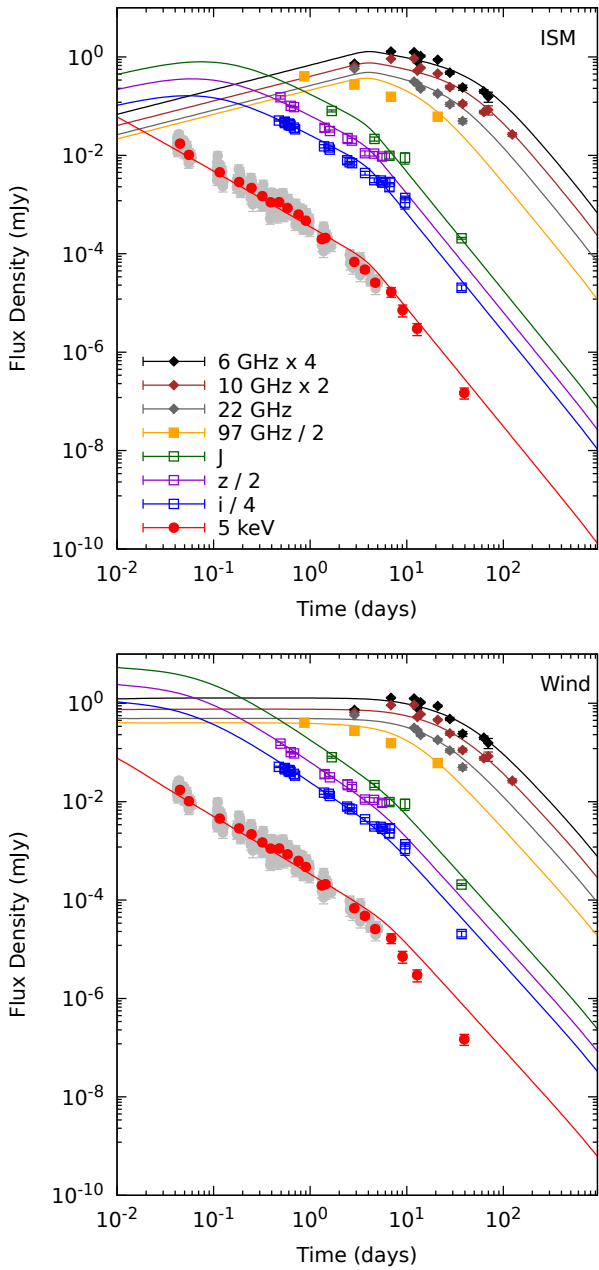


Figure 8. Analytical fits to the light curves for ISM- (top) and wind-type (bottom) CBM. The ISM fit is better at replicating the post-break slope.

time to a maximum of $2\pi(1 - \cos 1/\Gamma)$ of the total theoretical luminosity (e.g. Kumar & Zhang 2015). When the jet is ultra-relativistic, or $\Gamma \gg 1/\theta_j$, there is not enough time for the jet in its own frame to expand sideways. However, during the jet break, or where $\Gamma \sim 1/\theta_j$, the assumption breaks down and the jet is free to expand laterally. If this expansion proceeds at the sound speed, one should expect two breaks in the light curve, one that is geometric where $\Gamma \sim 1/\theta_j$, and the other for

sideways expansion when Γ drops to $1/(\sqrt{3}\theta_j)$ (Granot et al. 1999, 2000; Granot & Loeb 2001; Granot & Sari 2002; Piran 2004). Note that for a structured jet, this will change. In contrast, if the expansion is at the speed of light, both the breaks would coincide. However, one would need extremely fine light curve sampling to observe an effect such as this, which we do not have here, and the breaks will not be infinitely sharp, so they will be combined into one. Lateral expansion would result in an even further reduction in luminosity toward our line of sight due to expansion of the jet material itself (e.g. Rhoads 1999).

In the case of lateral expansion at an observing frequency $\nu > \nu_c > \nu_m$ or $\nu_c > \nu > \nu_m$, which is true for the post-break X-ray and optical light curves in this paper respectively (Figure 5), the expected post-break slope is p . From simple pre-break broken power law fits, numerical and analytical modelling, we could determine p to be in the range of 2.00-2.60. However, the *observed* post-break achromatic slope is -2.99 ± 0.10 (Figure 2) – higher at least by 6-7 σ than the p from model fits. Such steep slopes are relatively rare, although have been observed in few GRBs (e.g., Wang et al. 2018; Panaiteescu 2007) but with much larger errors (~ 0.5 in slope) making the detection much less certain. This is clearly not an obvious example of the kind of lateral expansion predicted by Rhoads (1999), which is not predicted to proceed this fast. Indeed, Zhang & MacFadyen (2009) show through hydrodynamic simulations that in many cases it may be incorrect to expect a simple p decay in the case of lateral expansion due to a number of more complex effects.

One of the primary conclusions from Zhang & MacFadyen (2009) remains that numerical simulations show that lateral expansion is much slower than what one expects from simple analytic theory as in Rhoads (1999), Sari et al. (1999) or Piran (2004). This partly stems from the fact that the jet ceases to be structureless (top-hat) at $\Gamma \sim 1/\theta_j$ and as it expands sideways. For an almost on-axis viewer (as we believe is the case for GRB 220101A from fitting models), the inclusion of time-lag effects from the off-axis would make the outer jet brighter than the inner as the off-axis radiation comes from a time when the jet was faster/had a higher energy density. This would create a limb-brightened jet (Granot et al. 1999; Zhang & MacFadyen 2009). A transition from a highly relativistic regime to a regime where $\Gamma < 1/\theta_j$ would hence be accompanied by a jet break but the post-break slope would strongly depend on the jet energy, viewing angle and the opening angle. This post-break slope would be independent of the presence of lateral expansion. It is hence clear that the analyt-

ical theory of lateral expansion agrees with numerical simulations to only a certain extent as discussed in e.g., Zhang & MacFadyen (2009), van Eerten & MacFadyen (2011) or Granot & Loeb (2001).

If the post-break slope was shallower than p , lateral expansion could have certainly been ruled out. However, since it is much steeper, lateral expansion cannot be ruled out, while the geometric edge effect alone can. Since a GRB is a rare event that does not “repeat”, we must make sure proper monitoring exists especially at late times for future GRBs, so that effects like this can be properly tested, unlike our case where the late-time sampling is imperfect.

4.2. Test of the standard model : radio behaviour, ξ and low n_0

The electron participation fraction, or ξ , can provide important clues regarding the nature of the burst and the circumburst medium. Our analyses in the previous section have shown that the afterglow emission can be equally well described by either of a top-hat or a Gaussian jet, with the latter having slightly higher energy requirements. Further, the best-fit including all data was found to have $\xi = 1.0$ for both jet structures. A top-hat jet at $\xi = 1.0$ was hence deemed the best model for the afterglow. However, the predicted (constant) CBM density was extremely low $< 10^{-4} \text{ cm}^{-3}$ (or IGM-like), for both `afterglowpy` (Tables 3, 4) and analytical fits (Table 7). While this issue does not exist for the wind-like CBM, the latter provided a much worse fit to the data compared to the ISM, especially the X-rays, as in Figure 8.

Further, upon ignoring the radio observations in the fit as in Figure 7, the resulting best-fit density n_0 was much higher (than with the radio), $> 0.01 \text{ cm}^{-3}$ at $\xi = 1.0$, which is still typically lower than expected ($\gtrsim 0.1 \text{ cm}^{-3}$, Ryden & Pogge 2021). All other parameters, including the energy budget, are either similar to that obtained previously and/or physically sound. The predicted radio emission in this case is almost 10 times higher than what is observed. For rare situations, low ISM densities $\sim 10^{-3} \text{ cm}^{-3}$ may be associated with galactic halos that may harbor short GRBs (e.g., de Barros et al. 2011). With lower ξ , as in as low as 0.01, the CBM density goes as high as 0.01 cm^{-3} , which implies n_0 should range between 10^{-5} and 0.01 cm^{-3} . Further, low CBM densities have been observed in many other GRBs previously (see e.g., Gompertz et al. 2018) – and it has been argued that strong reverse-shock features in the light curves, in particular, necessitate a relatively low circumburst density (e.g., Laskar et al. 2013, 2016; Alexander et al. 2017). It has been possible to find a set of best-fit parameters in

Gompertz et al. (2018) that would have a much lower ϵ_B with an increased n_0 , but situations like that were possible here only after making our priors smaller (e.g., increasing the lowest possible n_0).

Even with such a low density (and a very narrow jet, $\theta_j \simeq 0.6^\circ$), the analytical fit, mostly based on Granot & Sari (2002) and Rhoads (1999), furthermore fails to capture the full behavior of the afterglow. The radio and optical light curves are reproduced reasonably well, but the best fit places ν_c above 5 keV and, as a result, does not replicate the observed difference in the X-ray and optical pre-break slopes. As $\nu_c \propto n_0^{-1}$, this is a consequence of the low density required by the lower-frequency light curves. This is less of a problem in the `afterglowpy` fit (see Fig. 5).

It is hence unclear if the radio behaviour is not in accordance with the standard model, the reporting of very low ISM densities in GRBs incorporates a systematic error or if indeed a physical circumstance can produce ISM densities of $\lesssim 10^{-4} \text{ cm}^{-3}$ in the environments where GRBs are produced. We refer to the work of Kangas et al. (2020) and Kangas & Fruchter (2021), which have shown that the radio afterglow behaviour is very peculiar for a large number of LGRBs, and even when the radio is fit well, the inferred physical parameters are often at the edge of a physically plausible prior. Our work adds to that by demonstrating a possible issue of the standard model dealing with the radio fluxes, which are overpredicted by an order of magnitude when a physically plausible CBM density is obtained or are fit well when the CBM density is $\lesssim 10^{-4} \text{ cm}^{-3}$.

While the low density environment poses a challenge to the basic ISM model, we also point out that it may naturally arise in a “wind bubble” scenario (Castor et al. 1975; Weaver et al. 1977). In this scenario, the massive progenitor star of the GRB ejects a strong wind in its final stages of evolution. This wind clears a cavity around the progenitor, whose size is given by

$$R_{\text{bubble}} \simeq 20 \dot{M}_{-8}^{1/5} v_{w,8}^{2/5} n_{0,1}^{-1/5} t_{\star,7}^{3/5} \text{ pc} \quad (3)$$

(for a detailed discussion, see Pe’er & Wijers 2006; Pe’er & Ryde 2024). Here, $\dot{M} = 10^{-8} \dot{M}_{-8} M_\odot \text{ yr}^{-1}$ is the mass ejection rate from the star, $v_w = 10^8 v_{w,8} \text{ cm s}^{-1}$ is the wind velocity, $t_\star = 10^7 t_{\star,7} \text{ yr}$ is the lifetime of the wind ejection phase, and $n_0 = 10 n_{0,1} \text{ cm}^{-3}$ sets the default ambient (ISM) density to 10 cm^{-3} . For these parameters, the cavity density is indeed very low, and given by

$$n_{\text{cavity}} \simeq 10^{-5} \dot{M}_{-8}^{2/5} v_{w,8}^{-6/5} n_{0,1}^{3/5} t_{\star,7}^{-4/5}, \quad (4)$$

consistent with the values found here.

When the progenitor star explodes, the produced GRB blast wave then propagates into this low density cavity. For the fiducial parameters chosen, the total rest mass energy of cavity material, $E_{RM} = \dot{M}t_{\star}c^2 \approx 2 \times 10^{53} \dot{M}_{-8} t_{\star,7} \text{ erg}$ is less than the isotropically equivalent energy released in the explosion producing the GRB. In this scenario, the GRB jet will cross the cavity while still relativistic, maintaining its original (coasting) Lorentz factor. The typical observed time scale in which the jet will cross the cavity is $T^{ob} \sim R_{bubble}/\Gamma^2 c \sim 3 \text{ days}$, assuming $\Gamma = 100$; clearly, these values provide an order of magnitude estimation, and will vary based on the uncertain cavity size and GRB Lorentz factor.

Thus, the cavity scenario predicts an overall signal that is similar to that of an explosion into a low-density medium. The parameters chosen demonstrate that a cavity of several parsec size and very low density is plausible. A unique, a-chromatic signal may be observed when the blast wave crosses the cavity (Pe'er & Wijers 2006; Pe'er & Ryde 2024), but it may be difficult to detect (Nakar & Granot 2007; van Eerten et al. 2009).

5. CONCLUSIONS

1. GRB 220101A is one of the most energetic bursts ever detected, with $E_{\gamma, \text{iso}} \sim 3.6 \times 10^{54} \text{ erg}$ at a redshift of $z = 4.618$. The afterglow light curve shows a distinct steepening at $\gtrsim 8.6 \pm 0.1$ days from radio through X-rays, with a post-break slope close to $\sim 3.0 \pm 0.1$, which is $> 5\sigma$ steeper than the slope of p (2.50 from analytical spectral fitting) expected from simple lateral expansion theory of a top-hat jet. This hints at possibly more complex effects in play that include hydrodynamics and geometric effects (e.g., Zhang & MacFadyen 2009).
2. We fit model afterglow light curves for a top-hat and Gaussian jet using `afterglowpy` (Ryan et al. 2020) to better understand the physics of the GRB engine. We found that the case with the highest electron participation fraction $\xi = 1.0$ described the light curve and spectral behaviour the best, with physically feasible parameters enlisted in Tables 2-4, except the case of the CBM density, which was found to be $< 10^{-4} \text{ cm}^{-3}$ for the $\xi = 1.0$ case. Removal of the radio data from the fit significantly increased the density – by two orders of magnitude – with an overprediction of the radio in that case.
3. Similar behaviour is common in other LAT bursts (Gompertz et al. 2018), including GRB 160625B (Kangas et al. 2020), where the densities were similarly low. It is either possible that GRBs commonly inhabit large cavities in the IGM or the ra-

dio behaviour is peculiar and we do not have an explanation for the same using the standard model. However, while we are modeling a time-dependent source, the microphysics parameters are assumed to be static. It is hence worth exploring whether introducing a time dependency in some parameters could ameliorate the issues encountered in modeling radio afterglows.

4. A possible self-consistent explanation for such low ISM densities lies in the possible evacuation of the circumburst medium by strong winds launched by the GRB progenitor in the final stages of its evolution. The GRB jet is then expected to propagate into this low density cavity. Appropriate sets of physical parameters (like mass ejection rate, wind velocity or lifetime of the wind ejection phase) can in principle lead to ISM densities that are $\sim 10^{-5} \text{ cm}^{-3}$ (Equation 4). However, due to the parameter uncertainties involved (as discussed in the text), we cannot say for sure if the low densities are indeed due to progenitor winds or are a problem of the standard model.
5. It is possible we are seeing peculiar radio behaviour in the afterglow of GRB 220101A, as mentioned above. This ties in with the general absence of complete understanding of the radio emission from GRBs (see e.g., Rhodes et al. 2024). Furthermore, radio-loud and radio-quiet GRBs, as discussed in a number of previous studies (e.g., Hancock et al. 2013; Gompertz et al. 2018; Lloyd-Ronning et al. 2019; Lloyd-Ronning 2022), have been suggested to originate from different GRB progenitors, where the former possibly originates from a binary merger. Differences in the nature of progenitors necessarily include differences in the physical properties of these GRBs, e.g., the isotropic energies, spectral shapes, or the circumburst density profile. A larger CBM (ISM-like) density requires a much brighter-than-observed radio emission in the case of GRB220101A according to the standard fireball model. In contrast, if the radio flux level is predicted correctly by the standard model, the CBM densities become very low. It is possible this is related to a problem in the standard model, or that the progenitors of GRBs can accommodate wide differences in the properties of the circumburst medium profile (Fryer & Woosley 1998; Zhang & Fryer 2001; Lloyd-Ronning et al. 2019).

Parameter	With IC	Without IC	Zhu et al. (2023)
$\log(E_{\text{K,iso}}/\text{erg})$	$56.17^{+0.07}_{-0.05}$	$55.02^{+0.07}_{-0.07}$	$54.57^{+0.03}_{-0.03}$
p	2.16 ± 0.02	$2.14^{+0.02}_{-0.02}$	$2.44^{+0.01}_{-0.01}$
$\log(\theta_{\text{obs}}/\text{rad})$	-2.45 ± 0.04	-1.73 ± 0.05	$\theta_{\text{obs}} = 0$
$\log(\theta_j/\text{rad})$	-2.19 ± 0.03	$-1.46^{+0.04}_{-0.06}$	$-1.22^{+0.07}_{-0.08}$
$\log(n_0/\text{cm}^{-3})$	$-5.44^{+0.25}_{-0.33}$	$-0.88^{+0.27}_{-0.31}$	$-1.01^{+0.33}_{-0.39}$
$\log \epsilon_e$	$-1.38^{+0.11}_{-0.09}$	$-0.48^{+0.08}_{-0.07}$	$-0.51^{+0.02}_{-0.02}$
$\log \epsilon_B$	$-1.84^{+0.34}_{-0.31}$	$-4.03^{+0.41}_{-0.16}$	$-4.13^{+0.17}_{-0.37}$
A_B	$0.13^{+0.04}_{-0.02}$	$0.15^{+0.03}_{-0.03}$	
E_{K} (erg)	3.1×10^{51}	6.2×10^{51}	6.3×10^{51}
χ^2/DOF	2.1	2.0	

Table 8. Best-fit parameters for the Tophat jet for different values of ξ .

ARC acknowledges the support of the Department of Atomic Energy, Government of India, under the project 12-R&D-TFR-5.02-0700 and several pieces of advice from Geoffrey Ryan. TK acknowledges support from the Research Council of Finland project 360274. This paper makes use of the following ALMA data: ADS/JAO.ALMA#2021.1.00658.T. ALMA is a partnership of ESO (representing its member states), NSF (USA) and NINS (Japan), together with NRC (Canada), NSTC and ASIAA (Taiwan), and KASI (Republic of Korea), in cooperation with the Republic of Chile. The Joint ALMA Observatory is operated by ESO, AUI/NRAO and NAOJ. The National Radio Astronomy Observatory and Green Bank Observatory are facilities of the U.S. National Science Foundation operated under cooperative agreement by Associated Universities, Inc.

APPENDIX

A. COMPARISON WITH THE RESULTS OF ZHU ET AL.

`Afterglowpy` (with $\xi = 1.0$) fits to the same afterglow by Zhu et al. (2023), where the only difference was the absence of the final Chandra X-ray data point at ~ 40 days, show markedly different set of parameters, especially the inferred ISM number density, which was $\gtrsim 10^4$ times the one obtained using our fits. With the intention of examining this discrepancy, we fit our data starting from the Zhu et al. (2023) best-fit parameters for two spectral types inside `afterglowpy`, with and without inverse Compton losses. For the case where IC losses are ignored, the spectrum fits well with the Zhu et al. (2023) parameters ($\chi^2/\text{DOF} \simeq 2$) and the radio is well reproduced (Figure 9) with the number density “physical”. In contrast, for the more physically relevant scenario that includes IC losses, the radio fit is poor (and $\chi^2/\text{DOF} \simeq 9$) for a low walker-step pair (300, 2000), with higher density values still, implying the Zhu et al. (2023) parameters did not form the global minima. For a longer and larger run, the simulation converges to the values we have obtained in the main sections of the paper, which is expected.

Table 8 shows the best-fit parameters for our run with IC losses, the parameters without IC losses, and the parameters from Zhu et al. (2023) in three separate columns. It is possible the question therefore partly boils down to inclusion of IC losses in the fits. However, from a purely physical standpoint, it would be unwise to ignore IC losses, howsoever

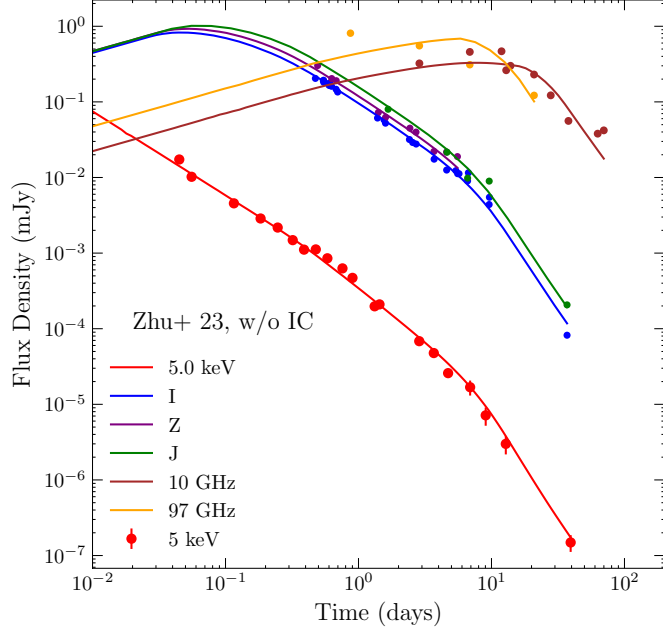


Figure 9. Afterglow light curve of GRB 220101A with the initial parameters taken from Zhu et al. (2023) and run for 300 walkers and 2000 steps. The best-fitting `afterglowpy` model is shown in solid lines when inverse Compton losses are ignored.

Parameter	Without Radio	With Radio
$\log(E_{K,\text{iso}}/\text{erg})$	$55.61^{+0.27}_{-0.28}$	$55.10^{+0.10}_{-0.10}$
p	$2.01^{+0.27}_{-0.01}$	$2.28^{+0.04}_{-0.02}$
$\log(\theta_{\text{obs}}/\text{rad})$	$-1.66^{+0.15}_{-0.15}$	$-2.02^{+0.07}_{-0.06}$
$\log(\theta_j/\text{rad})$	$-1.06^{+0.09}_{-0.36}$	$-1.46^{+0.06}_{-0.06}$
$\log(n_0/\text{cm}^{-3})$	$-0.95^{+0.47}_{-3.69}$	$-4.98^{+0.09}_{-0.02}$
$\log \epsilon_e$	$-0.65^{+0.18}_{-0.38}$	$-0.54^{+0.04}_{-0.04}$
$\log \epsilon_B$	$-2.46^{+0.46}_{-0.46}$	$-3.10^{+0.15}_{-0.15}$
A_V	$1.00^{+0.00}_{-0.91}$	$0.07^{+0.01}_{-0.01}$
E_K (erg)	1.5×10^{53}	7.5×10^{51}
χ^2/DOF	7.9	2.1

Table 9. Best-fit parameters for models with and without radio data for GRB160625B.

physical a parameter space one might obtain by ignoring IC losses. We compared our results with that of Zhu et al. (2023) to only throw light on the parameter discrepancies for the same source.

B. THE AFTERGLOW OF GRB 160625B

Similar peculiar ISM density behaviour in GRB 160625B had been observed as well. Here we ran `afterglowpy` fits (with 300 walkers and 3000 steps) to the afterglow of the source for $\xi = 1.0$, with and without the radio data.

Figure 10 shows the difference in fits for $\xi = 1.0$ when the radio is considered and when it is not. Parameter results have been tabulated below in Table 9. The issues are very similar to GRB220101A: extremely low n_0 when the radio is included and a “physical” n_0 when excluded with ~ 100 times overprediction of the radio flux densities.

REFERENCES

Alexander, K. D., Laskar, T., Berger, E., et al. 2017, ApJ, 848, 69, doi: [10.3847/1538-4357/aa8a76](https://doi.org/10.3847/1538-4357/aa8a76)

Burns, E., Svinkin, D., Fenimore, E., et al. 2023, ApJL, 946, L31, doi: [10.3847/2041-8213/acc39c](https://doi.org/10.3847/2041-8213/acc39c)

Castor, J., McCray, R., & Weaver, R. 1975, ApJL, 200, L107, doi: [10.1086/181908](https://doi.org/10.1086/181908)

Cunningham, V., Cenko, S. B., Ryan, G., et al. 2020, ApJ, 904, 166, doi: [10.3847/1538-4357/abc2cd](https://doi.org/10.3847/1538-4357/abc2cd)

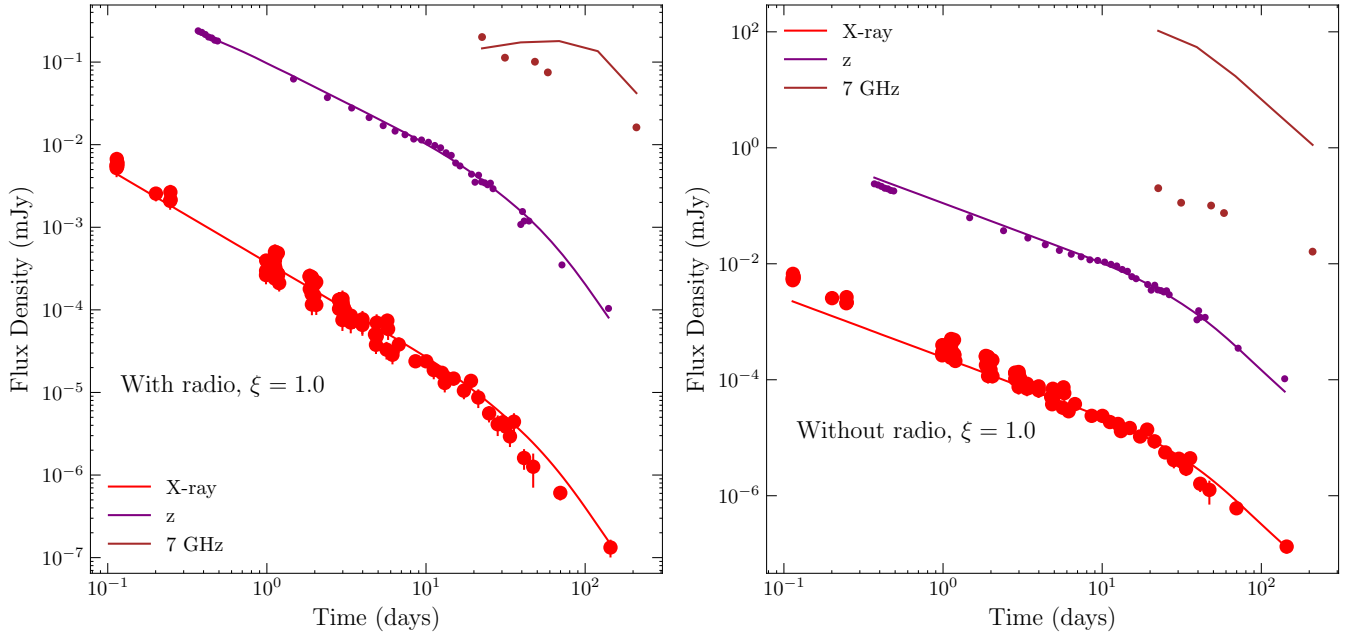


Figure 10. Afterglow light curve of GRB 160625B with the best-fitting `afterglowpy` model including and excluding the radio data in the left and right panels respectively. Exclusion of the radio data shows strong overprediction (~ 100 times) of the observed radio flux densities.

Daly, R. A., & Marscher, A. P. 1988, *ApJ*, 334, 539, doi: [10.1086/166858](https://doi.org/10.1086/166858)

D'Avanzo, P., Melandri, A., Covino, S., et al. 2022a, GRB Coordinates Network, 31373, 1

D'Avanzo, P., Melandri, A., Fugazza, D., et al. 2022b, GRB Coordinates Network, 31395, 1

de Barros, G., Amati, L., Bernardini, M. G., et al. 2011, *A&A*, 529, A130, doi: [10.1051/0004-6361/201116659](https://doi.org/10.1051/0004-6361/201116659)

de Ugarte Postigo, A., Kann, D. A., Thoene, C. C., et al. 2022, GRB Coordinates Network, 31358, 1

Evans, P. A., Beardmore, A. P., Page, K. L., et al. 2007, *A&A*, 469, 379, doi: [10.1051/0004-6361:20077530](https://doi.org/10.1051/0004-6361:20077530)

—. 2009, *MNRAS*, 397, 1177, doi: [10.1111/j.1365-2966.2009.14913.x](https://doi.org/10.1111/j.1365-2966.2009.14913.x)

Foreman-Mackey, D., Hogg, D. W., Lang, D., & Goodman, J. 2013, *PASP*, 125, 306, doi: [10.1086/670067](https://doi.org/10.1086/670067)

Fryer, C. L., & Woosley, S. E. 1998, *ApJL*, 502, L9, doi: [10.1086/311493](https://doi.org/10.1086/311493)

Fu, S. Y., Zhu, Z. P., Xu, D., Liu, X., & Jiang, S. Q. 2022, GRB Coordinates Network, 31353, 1

Fynbo, J. P. U., de Ugarte Postigo, A., Xu, D., et al. 2022, GRB Coordinates Network, 31359, 1

Gompertz, B. P., Fruchter, A. S., & Pe'er, A. 2018, *ApJ*, 866, 162, doi: [10.3847/1538-4357/aadb8](https://doi.org/10.3847/1538-4357/aadb8)

Granot, J., & Loeb, A. 2001, *ApJL*, 551, L63, doi: [10.1086/319843](https://doi.org/10.1086/319843)

Granot, J., Piran, T., & Sari, R. 1999, *ApJ*, 513, 679, doi: [10.1086/306884](https://doi.org/10.1086/306884)

—. 2000, *ApJL*, 534, L163, doi: [10.1086/312661](https://doi.org/10.1086/312661)

Granot, J., & Sari, R. 2002, *ApJ*, 568, 820, doi: [10.1086/338966](https://doi.org/10.1086/338966)

Hancock, P. J., Gaensler, B. M., & Murphy, T. 2013, *ApJ*, 776, 106, doi: [10.1088/0004-637X/776/2/106](https://doi.org/10.1088/0004-637X/776/2/106)

Kangas, T., & Fruchter, A. S. 2021, *ApJ*, 911, 14, doi: [10.3847/1538-4357/abe76b](https://doi.org/10.3847/1538-4357/abe76b)

Kangas, T., Fruchter, A. S., Cenko, S. B., et al. 2020, *ApJ*, 894, 43, doi: [10.3847/1538-4357/ab8799](https://doi.org/10.3847/1538-4357/ab8799)

Kumar, P., & Zhang, B. 2015, *PhR*, 561, 1, doi: [10.1016/j.physrep.2014.09.008](https://doi.org/10.1016/j.physrep.2014.09.008)

Laskar, T., Berger, E., Zauderer, B. A., et al. 2013, *ApJ*, 776, 119, doi: [10.1088/0004-637X/776/2/119](https://doi.org/10.1088/0004-637X/776/2/119)

Laskar, T., Alexander, K. D., Berger, E., et al. 2016, *ApJ*, 833, 88, doi: [10.3847/1538-4357/833/1/88](https://doi.org/10.3847/1538-4357/833/1/88)

Lloyd-Ronning, N. 2022, *ApJ*, 928, 104, doi: [10.3847/1538-4357/ac54b3](https://doi.org/10.3847/1538-4357/ac54b3)

Lloyd-Ronning, N. M., Gompertz, B., Pe'er, A., Dainotti, M., & Fruchter, A. 2019, *ApJ*, 871, 118, doi: [10.3847/1538-4357/aaf6ac](https://doi.org/10.3847/1538-4357/aaf6ac)

Markwardt, C. B., Barthelmy, S. D., Krimm, H. A., et al. 2022, GRB Coordinates Network, 31369, 1

Mészáros, P., & Rees, M. J. 1999, *MNRAS*, 306, L39, doi: [10.1046/j.1365-8711.1999.02800.x](https://doi.org/10.1046/j.1365-8711.1999.02800.x)

Nakar, E., & Granot, J. 2007, *MNRAS*, 380, 1744, doi: [10.1111/j.1365-2966.2007.12245.x](https://doi.org/10.1111/j.1365-2966.2007.12245.x)

Nicuesa Guelbenzu, A., Melnikov, S., Klose, S., Stecklum, B., & Ludwig, F. 2022, GRB Coordinates Network, 31401, 1

Panaitescu, A. 2007, MNRAS, 380, 374, doi: [10.1111/j.1365-2966.2007.12084.x](https://doi.org/10.1111/j.1365-2966.2007.12084.x)

Pe'er, A., & Ryde, F. 2024, arXiv e-prints, arXiv:2406.03841, doi: [10.48550/arXiv.2406.03841](https://doi.org/10.48550/arXiv.2406.03841)

Pe'er, A., & Wijers, R. A. M. J. 2006, ApJ, 643, 1036, doi: [10.1086/500969](https://doi.org/10.1086/500969)

Pei, Y. C. 1992, ApJ, 395, 130, doi: [10.1086/171637](https://doi.org/10.1086/171637)

Perley, D. A. 2022a, GRB Coordinates Network, 31357, 1

—. 2022b, GRB Coordinates Network, 31425, 1

Piran, T. 2004, Reviews of Modern Physics, 76, 1143, doi: [10.1103/RevModPhys.76.1143](https://doi.org/10.1103/RevModPhys.76.1143)

Rhoads, J. E. 1999, ApJ, 525, 737, doi: [10.1086/307907](https://doi.org/10.1086/307907)

Rhodes, L., van der Horst, A. J., Bright, J. S., et al. 2024, MNRAS, 533, 4435, doi: [10.1093/mnras/stae2050](https://doi.org/10.1093/mnras/stae2050)

Ryan, G., van Eerten, H., Piro, L., & Troja, E. 2020, ApJ, 896, 166, doi: [10.3847/1538-4357/ab93cf](https://doi.org/10.3847/1538-4357/ab93cf)

Ryden, B. S., & Pogge, R. W. 2021, Interstellar and intergalactic medium (Cambridge University Press), doi: [10.1017/9781108781596](https://doi.org/10.1017/9781108781596)

Sari, R., & Esin, A. A. 2001, ApJ, 548, 787, doi: [10.1086/319003](https://doi.org/10.1086/319003)

Sari, R., Piran, T., & Halpern, J. P. 1999, ApJL, 519, L17, doi: [10.1086/312109](https://doi.org/10.1086/312109)

Tohuvavohu, A., Groppi, J. D., Kennea, J. A., et al. 2022, GRB Coordinates Network, 31347, 1

Tsvetkova, A., Frederiks, D., Lysenko, A., et al. 2022, GRB Coordinates Network, 31433, 1

van Eerten, H., van der Horst, A., & MacFadyen, A. 2012, ApJ, 749, 44, doi: [10.1088/0004-637X/749/1/44](https://doi.org/10.1088/0004-637X/749/1/44)

van Eerten, H. J., & MacFadyen, A. I. 2011, ApJL, 733, L37, doi: [10.1088/2041-8205/733/2/L37](https://doi.org/10.1088/2041-8205/733/2/L37)

van Eerten, H. J., Meliani, Z., Wijers, R. A. M. J., & Keppens, R. 2009, MNRAS, 398, L63, doi: [10.1111/j.1745-3933.2009.00711.x](https://doi.org/10.1111/j.1745-3933.2009.00711.x)

Vinko, J., Pal, A., Kriskovics, L., Szakats, R., & Vida, K. 2022, GRB Coordinates Network, 31361, 1

Wang, X.-G., Zhang, B., Liang, E.-W., et al. 2018, ApJ, 859, 160, doi: [10.3847/1538-4357/aabc13](https://doi.org/10.3847/1538-4357/aabc13)

Weaver, R., McCray, R., Castor, J., Shapiro, P., & Moore, R. 1977, ApJ, 218, 377, doi: [10.1086/155692](https://doi.org/10.1086/155692)

Zhang, W., & Fryer, C. L. 2001, ApJ, 550, 357, doi: [10.1086/319734](https://doi.org/10.1086/319734)

Zhang, W., & MacFadyen, A. 2009, ApJ, 698, 1261, doi: [10.1088/0004-637X/698/2/1261](https://doi.org/10.1088/0004-637X/698/2/1261)

Zhu, Z.-P., Lei, W.-H., Malesani, D. B., et al. 2023, ApJ, 959, 118, doi: [10.3847/1538-4357/ad05c8](https://doi.org/10.3847/1538-4357/ad05c8)